Edge plasma transport and microstability analysis with lithium-coated plasma-facing components in NSTX

J.M. Canik[1], W. Guttenfelder[2], R. Maingi[1], T.H. Osborne[3], S. Kubota[4], Y. Ren[2], R.E. Bell[2], H.W. Kugel[2], B.P. LeBlanc[2], V.A. Souhkanovskii[5]

[1] Oak Ridge National Laboratory, Oak Ridge, TN 37831, USA
[2] Princeton Plasma Physics Laboratory, Princeton University, Princeton, NJ 08543, USA
[3] General Atomics, San Diego, CA, 92186, USA
[4] University of California-Los Angeles, Los Angeles, CA 90095, USA
[5] Lawrence Livermore National Laboratory, Livermore, CA 94551, USA
E-mail contact of main author: canikjm@ornl.gov

Abstract. The pedestal structure in NSTX is strongly affected by lithium coatings applied to the PFCs. In discharges with lithium, the density pedestal widens, and the electron temperature (T_e) gradient increases inside a radius of $\psi_N \sim 0.95$, but is unchanged for $\psi_N > 0.95$. Interpretive 2-D plasma/neutrals modeling has been performed for pre-lithium and with-lithium discharges. The inferred effective electron thermal (χ_e^{eff}) and particle (D_e^{eff}) profiles reflect the profile changes: χ_e^{eff} is similar in the near-separatrix region, and is reduced in the region $\psi_N < 0.95$ in the with-lithium case. The D_e^{eff} profile shows a broadening of the region with low diffusivity with lithium, while the minimum value within the steep gradient region is comparable in the two cases. The linear microstability properties in the near-separatrix and pedestal-top regions have been analyzed. At the pedestal top microtearing modes are unstable without lithium. These are stabilized and become TEM-like with lithium, with growth rates reduced and comparable to ExB shearing rates. In the region $\psi_N > 0.95$, both the pre- and with-lithium cases are calculated to be unstable to ETG modes, with higher growth rates with lithium. Both cases are also found to lie near the onset for kinetic ballooning modes, but in the second stable region where growth rates decrease with increasing pressure gradient.

1. Introduction

The application of lithium coatings to the plasma-facing components (PFCs) of the National Spherical Torus Experiment (NSTX) has been shown to dramatically alter the plasma behavior, leading to a reduction in divertor particle recycling [1], increased energy confinement [2], and at high lithium levels the complete elimination of edge-localized modes (ELMs) [3]. The plasma edge in particular shows a marked change with lithium coatings applied, with a widening of the pressure pedestal observed [4] that leads to an overall increase in the pedestal-top pressure, contributing to the observed improvement in energy confinement. While the improvements in plasma performance are potentially advantageous for future device, the physics underlying the observed changes has not been established, making extrapolation uncertain. Here we present an exploration of possible mechanisms involved, through calculations of the linear microstability of NSTX discharges without and with lithium coatings, motivated by interpretive 2-D plasma/neutral modeling of the edge transport.

1.1 Summary of 2-D modeling results

2-D modeling of pre-lithium and with-lithium discharges has been performed using the SOLPS suite of codes [5], which solves a set of coupled fluid plasma and kinetic neutral transport equations. The modeling is interpretive, with the "anomalous" cross-field transport coefficients adjusted until agreement is obtained between the measured and modeled midplane density and temperature profiles (divertor heat flux and D_α measurements also constrain the modeling). The power flowing from the core into the edge is input as a boundary condition, and the sources due to neutral recycling are calculated self-consistently. This technique yields "effective" cross-field diffusivities (no attempt is made to discern any

convective particle transport), along with the particle recycling coefficient R at the PFC surfaces [6].

A summary of the 2-D modelling results for plasmas without and with lithium coated PFCs is shown in Figure 1 (a comprehensive presentation of the modeling approach and results can be found in [7]). The modeling indicates that the application of lithium reduces R from ~0.98 to 0.9 [6]. The modeled and measured pedestal profiles (Figure 1) show that, with lithium coatings, the electron density (n_e) gradient within the pedestal is reduced by ~50%, which is consistent with the reduction in particle source with lithium [7]. The width of the n_e pedestal increases, however, so that the pedestal-top n_e is comparable in the two cases. The electron temperature (T_e) profile is similar pre- and with-lithium in the region $\psi_N > 0.95$, while the T_e gradient is stronger inside this radius for the with-lithium case. The interpretive effective electron thermal (χ_e^{eff}) and particle (D_e^{eff}) profiles reflect these profile changes: χ_e^{eff} is similar outside ψ_N ~0.95, and is reduced in the region $\psi_N<0.95$ as the amount of lithium increases. The D_e^{eff} profile shows a broadening of the region with low diffusivity with lithium, while the minimum value within the steep gradient region is comparable in the various cases. These changes reflect the widening of the pressure pedestal observed with lithium.

The 2-D modeling highlights two edge regions with differing behavior as lithium is applied. In the far edge outside ψ_N~0.95, the T_e profile is approximately unchanged by the application of lithium. The near-constancy of the T_e gradient is observed over a wide range of lithium deposition amounts [7], and in spite of the strong changes in the n_e profile that occur with lithium. This facet of the edge profiles is important to the changes in ELM behaviour observed with lithium: since T_e is unchanged while the n_e profile is reduced, the pressure gradient and bootstrap current in this region is reduced. Stability calculations with the ELITE code [8] have shown that this reduces the drive of the peeling component of peeling-ballooning stability [4], resulting in increased stability with lithium, consistent with the experimental trends of ELM behaviour [9].

In the pedestal-top region inside a radius of ψ_N~0.95, the effective transport coefficients are reduced as lithium is applied. The electron thermal diffusivity shows a continuous reduction in this region as more lithium is deposited, to the point that a transport barrier is difficult to make out in the maximum lithium case. The particle diffusivity, on the other hand, shows a broadening of the barrier region as lithium is increased, reflecting the measured widening of the n_e pedestal [9].

Turbulence measurements have also been made in these two regions [7]. In the edge region, reflectometry indicates a strong reduction in low-k fluctuations, suggesting a change in the underlying nature of the turbulence. At the pedestal top, high-k microwave scattering measurements show a reduction in fluctuation levels at electrons scales, consistent with the inferred reduced transport.
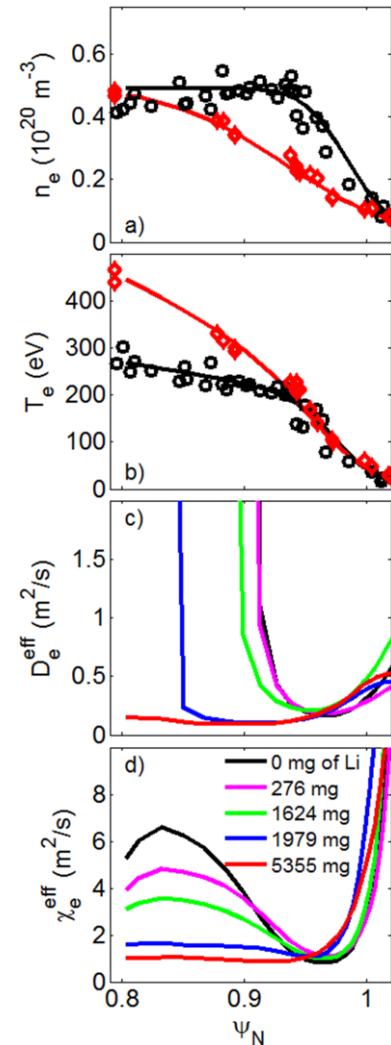

FIG 1. Profiles of a) n_e, b) T_e, without (black) and with 5355 mg of lithium (red), and c) D_e^{eff} and d) χ_e^{eff} as amount of lithium is varied

1.2 Microstability analysis with GS2

The linear microstability properties of these edge plasmas have been analyzed using the initial value gyrokinetic code GS2 [10]. The purpose of this study is to explore the physics behind the transport changes observed in the two regions highlighted by 2-D modeling, i.e., to understand why the T_e gradient is fixed at the edge, and why transport is reduced inside ψ_N~0.95. Two types of instabilities are of special interest: kinetic ballooning modes (KBM), which have gained interest in the community recently as possibly limiting the pedestal pressure gradient between ELMs [11], and electron temperature gradient modes (ETG), which may play a role in the observed stiffness of the T_e profile for $\psi_N > 0.95$ [7].

Radial profiles of the normalized pressure gradient (shown in terms of $\beta=2\mu_0 p/B_0^2$) are shown in Figure 2, as well as the ratio of the minimum gradient scale length L to the ion gyroradius ρ_i. At the pedestal top, where the pressure gradient (panel a) is relatively small compared to its peak value, $L/\rho_i \sim 20\text{-}40$. The ordering $\rho_i/L << 1$ assumed in the local analysis presented here is therefore marginal at this location, and global effects are likely to quantitatively alter the results [12]. In the steep gradient region nearer the separatrix, L/ρ_i is reduced further to ~5, indicating that non-local effects are likely to be strong.

FIG 2. Profiles of a) pressure gradient, b) ratio of gradient scale length to ion gyroradius without (black) and with (red) lithium

With such large values of ρ_i/L, it is also possible that $\delta f/f$ is no longer small, and a full-f code should be used. Nonetheless, the results presented here provide a first qualitative look at the dominant instabilities and how they trend with quantities that are known to change with lithium; the consequences of this local approach are discussed in more detail in Section 3. For electron scale instabilities (i.e., the ETG analysis presented here), however, $\rho_e/L << 1$ is well satisfied.

2. Survey of linear microstability properties without and with lithium

The linear microstability characteristics of the plasma edge profiles have been examined for the end-cases shown in Figure 1 (without lithium and with maximum lithium deposition). Realistic magnetic geometries were used, based on kinetic equilibrium reconstructions including both the pedestal pressure profile and the bootstrap current, generated as part of edge peeling-ballooning analysis [4]. The calculations are fully electromagnetic, including both $\delta A_{\parallel}$ and $\delta B_{\parallel}$, and pitch-angle scattering collisions are included. In all calculations, the plasma profiles are taken from pedestal profile fits used in peeling-ballooning analysis [4], with three plasma species included: electrons, deuterons, and fully stripped carbon ions. While not discussed here, extensive resolution scans have been performed to ensure convergence with respect to, e.g., number of poloidal grid points, poloidal extent of the grid, and time step, for the calculations presented here.

2.1 Dominant modes at $k_{\theta}\rho_s \lesssim 1$

For each plasma radius studied, linear growth rates are calculated over a range of $k_{\theta}\rho_s$. Using the GS2 initial value approach, this yields the growth rate of the most unstable mode, if multiple instabilities are present. The results are summarized in Figure 3, which shows radial profiles of the maximum growth rate from the $k_{\theta}\rho_s$ spectrum calculated at each radius. In this case, the $k_{\theta}\rho_s$ range is restricted to $k_{\theta}\rho_s \leq 1.0$ (electron scale microstability is presented
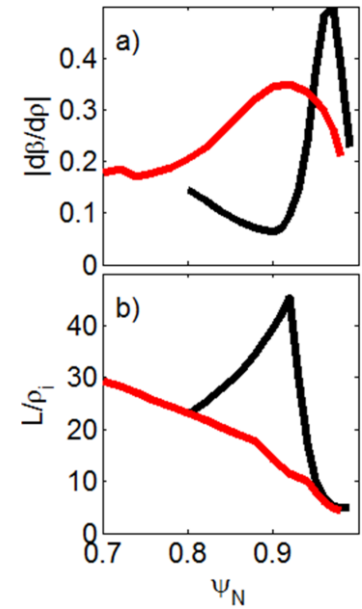
below). The type of mode is identified for different regions in the figure (ITG: ion temperature gradient; TEM: trapped electron; MT: microtearing; KBM: kinetic ballooning). The modes were identified based on parameter scans around the nominal operating point (described below), the sign of the real frequency, and by the eigenfunction structure in the case of MT [13] and KBM [14]. Also shown is the ExB shearing rate $\gamma_E=-(r/q)\partial/\partial r(E_r/RB_p)$, calculated based on the measured C^{6+} toroidal velocity and pressure profiles (although poloidal rotation is not included here, analysis of other discharges suggests that it is a small contributor to the total radial electric field [15]).

For the no-lithium pedestal, four distinct regions can be identified. Beginning with the outermost, the region at the foot of the pedestal near the separatrix is unstable to KBM-like modes, with growth rates that are much larger than the shear rates. Within the pedestal, where the pressure gradient is large, TEM is dominant (more precisely, a hybrid TEM/KBM mode very sensitive to β_e [16]), with growth rates reduced to within a factor of ~2 of the shear rate. At the pedestal top (near the inflection point in the n_e and T_e profiles), the dominant mode is MT, once

FIG 3. Profiles of a) growth rate (solid) and ExB shear rate (dashed), and b) real frequency of the most unstable mode with $k_\theta\rho_s \leq 1$ without (black) and with (red) lithium

more with growth rates much larger than the shear rate. Finally, inside the pedestal region (near the core), ITG is dominant. With lithium, the radial structure of the growth rates is qualitatively similar, but with broader corresponding radial regions due to the overall widening of the pedestal. In this case, however, the dominant instability for all three edge-most regions is a TEM/KBM hybrid (see the discussion in Section 3).

2.2 Scaling of dominant instabilities

The scaling of the dominant modes in several of the regions highlighted in Section 2.1 with various parameters (gradient scale lengths, collisionality, etc.) have been studied in order to determine the dominant mode type, as well as to help identify the mechanism behind the changes as lithium is applied. Figure 4 shows the scaling of the $k_\theta\rho_s=1.0$ growth rate for $\psi_N=0.93$ in the discharge without lithium (at the pedestal-top where MT is dominant) with density gradient and with the electron-ion collision frequency [14]. For each point in the density gradient scan, the pressure gradient of the local magnetic equilibrium has been adjusted to be consistent with the kinetic profiles
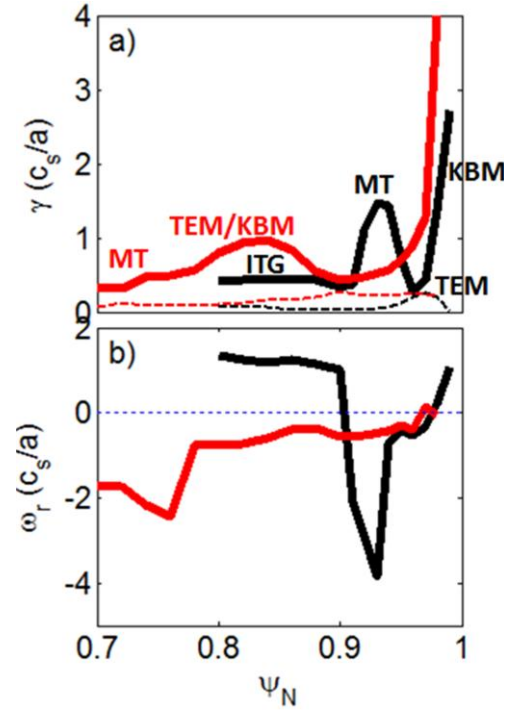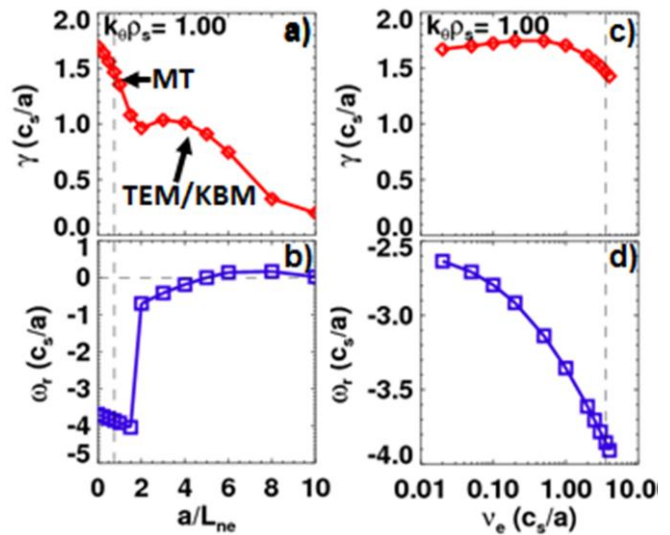

FIG 4. Scaling of growth rate and real frequency with a,b) density gradient and c,d) collisionality for $\psi_N=0.93$ without lithium

according to $\partial\beta/\partial r=\beta_e\Sigma_s n_s T_s(a/L_{ns}+a/L_{Ts})$ (see, e.g., [14]). The nominal experimental values are indicated by the vertical dashed lines. For this region, increasing the density gradient is stabilizing to the dominant MT instability (this is partially due to the stabilizing influence of the pressure gradient on the geometry [17]), allowing TEM/KBM hybrid mode to become dominant at higher density gradients, with much reduced growth rates at the $a/L_{ne} \sim 10$ measured at the same radius in the case with lithium. It thus appears that, with ELMs avoided with lithium, the density and pressure gradient at the pedestal top increase and strongly stabilize the MT modes dominant there, allowing the pedestal to continue to grow inwards (this is a similar qualitative picture to that reported based on analysis of MAST plasmas [13]). At this radius, the MT mode depends weakly on collisionality, and is modestly stabilized with increasing ν_e (panel c).

Figure 5 shows the scaling with electron temperature gradient and with pressure gradient of the dominant mode in the with-lithium case at a radius of $\psi_N=0.92$ (in terms of relative position within the pedestal, this location is similar to the steep-gradient region at $\psi_N=0.97$ without lithium). Increasing the T_e gradient is strongly destabilizing when scaled alone, and shows a sharp up-turn at high gradient that is due to KBM onset. When $\partial\beta/\partial r$ of the geometry is scaled consistently with the T_e gradient the destabilization is much weaker and the transition to KBM does not occur. The stabilizing influence of $\partial\beta/\partial r$ in the equilibrium is seen by scaling it alone (panel c, red curves). When β_e of the profiles is scaled

FIG 5. Scaling with a,b) electron temperature gradient and c,d) pressure gradient used in equilibrium for $\psi_N=0.92$ with lithium. Parameters are scanned individually (red) or consistently between geometry and profiles (black)

consistently with the $\partial\beta/\partial r$ (panel c, black curves), the dependence is again much weaker Even with β_e scaled consistently, however, increasing pressure gradient remains stabilizing at the experimental parameters.

2.3 ETG stability

It has been suggested that ETG modes could play a role in the transition from no-lithium to strong lithium deposition [7], in particular in the region outside $\psi_N\sim0.95$ where the T_e profile is observed to be rather stiff. To explore this possibility, the stability of electron-scale modes with $k_\theta\rho_s \geq 10.0$ has been calculated. ETG modes are calculated to be unstable in the region of interest ($\psi_N>0.95$) for both the without- and with-lithium cases, and stable elsewhere in the edge. Further, the growth rates increase substantially with lithium (normalized values increase by a factor of ~4. This is due to the change in profiles in this region that occur with lithium: ∇T_e is relatively unchanged while ∇n_e is reduced a factor of ~2, so that η_e is significantly higher, leading to stronger ETG instability. The change in ETG growth rates suggest that transport due to this mode would be a stronger contributor with lithium, and that it could be that without lithium, ETG transport is negligible, and becomes stronger as lithium is added, preventing ∇T_e from increasing even though n_e is lower. Non-linear simulations of the ETG transport are underway to test if it is quantitatively large enough to be consistent with such a picture.
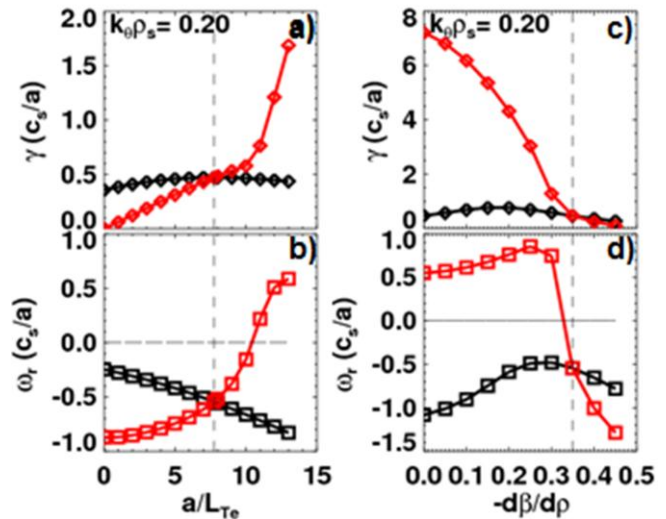
3. Ballooning stability

Given the success of the EPED model [11], in which KBMs are assumed to limit the pedestal pressure gradient between ELMs, in predicting the pedestal height and width over a range of experiments [18], the KBM is a considered a leading candidate for dominating pedestal transport. In light of this, the ballooning stability of NSTX discharges has been studied in detail. Calculations have been performed of ideal, infinite-n ballooning stability, which KBM is expected to follow for the most part, along with gyrokinetic calculations of KBM stability.

3.1 Ideal ballooning calculations

The infinite-n, ideal ballooning stability [19] has been calculated for the without- and with-lithium cases described above, with the results summarized in Figure 6. In this figure, the 'first stability' curve is the value pressure gradient at which the ballooning stability boundary is reached (starting from no gradient). The plasma is unstable to ballooning modes between this and the 'second stability' boundary, above which the modes are stable [20]. At some radii instability is never reached; this is due to the magnetic shear $s=(r/q)(dq/dr)$ in the experimental reconstruction being lower than the minimum value at which ballooning instability is calculated (see, e.g., Figure 7). To estimate the ballooning limit in this case, even though it can't strictly be reached without changing the shear, a third curve is added, which is the pressure gradient at ballooning mode onset at the minimum-shear point at which instability is predicted. The shear in the equilibrium as well as the shear at the minimum-shear point on the ballooning boundary is shown in panels b and d.

The calculations show that only for the very edge of the plasma, $\psi_N \geq 0.98$, is the experimental pressure gradient near the first stability boundary. Inside this radius, ballooning modes are stable for all pressure gradients at the experimental level of shear, indicating that second stability effects are strong. Thus, the ideal calculations indicate that ballooning modes can't

limit pressure gradient except for very near the separatrix. The experimental shear contains uncertainty, since the bootstrap current is calculated from a model [21] rather than measured. With the experimental profiles above the pressure gradient at minimum shear for instability for a sizable fraction of the pedestal region, this uncertainty could be the cause of the calculated stability. However, it should be noted that more recent calculations suggest that the bootstrap current model used here underestimates the current in spherical tokamaks [22], and so the shear could in reality be even lower that shown here, further increasing stability to ballooning modes.
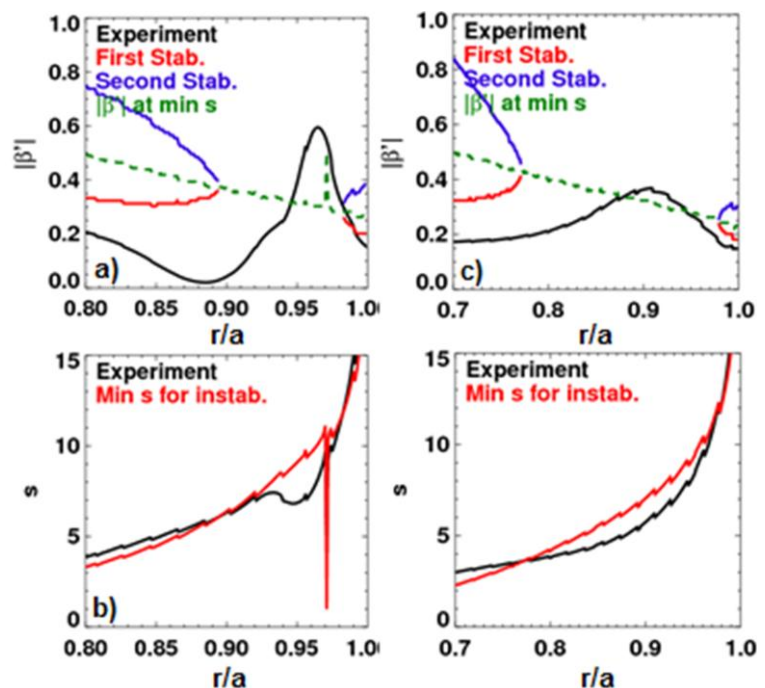
FIG 6. Profiles of experimental pressure gradient and ballooning boundaries a) without and d) with lithium; experimental shear and minimum shear for ballooning instability b) without and d) with lithium

3.2 Calculations of KBM stability

The stability of kinetic ballooning modes has been calculated using GS2. To explore stability space, calculations are performed over a range of magnetic shear and pressure gradient, for a fixed radius and $k_\theta \rho_s$. In this scan, the pressure gradient in the equilibrium and β_e in the profiles are scaled together consistently. Figure 7 shows an example of the calculated growth rates and real frequency in this 2D space, for the with-lithium case at a radius of ψ_N=0.94. The ideal boundary is also shown.

The growth rate contours largely follow the ideal ballooning boundary, with the maximum growth rate occurring close to the first stability boundary and rapidly falling off as the pressure gradient is increased towards second stability. The real frequency closely tracks the ideal boundary, with frequencies changing from negative to positive near the boundary. Based on the parity [13] and real vs. imaginary phasing of $\delta A_\parallel$ [14], regions with negative real frequencies are identified as TEM, and positive correspond with KBM being the dominant instability. Thus, in this case the KBM-unstable region corresponds very closely with the ideal calculations. While kinetic effects are expected to expand the KBM-unstable region

FIG 7. Contours of a) growth rate and b) real frequency vs. pressure gradient and shear ψ_N=0.94. Crosses indicate experimental values

somewhat [23], since the initial value approach used here only yields the most unstable mode, it may be that KBM is unstable outside this region but sub-dominant to TEM. The smooth variation of the real frequency with both the shear and pressure gradient suggest that this is a hybrid TEM-KBM mode [16] (similar to ITG-KBM modes identified in [14]), rather than two discrete branches that are competing for dominance. As noted in Section 2.2, increasing pressure gradient is stabilizing at experimental parameters. Similar results are obtained for the case without lithium, with KBM stability following the ideal boundary, and TEM smoothly transitioning to KBM as parameters are varied.

These gyrokinetic calculations, along with the ideal calculations, do not support the notion that KBMs limit the pedestal pressure gradient. Ballooning modes are calculated to be in the second stable regime for most of the pedestal, and growth rates are predicted to decrease with increasing pressure gradient, in conflict with the usual picture of KBMs as stiffly limiting the pressure gradient [18]. However, it should be noted that these calculations are local and do not include profile effects. It is possible that non-local effects in the gyrokinetic calculations would close off access to the second stable regime in a way that is not captured here, similar to the reduced access to second stability observed in finite-n MHD calculations compared to infinite-n [24]. In the future, global gyrokinetic calculations will be used to study this effect (the need for such calculations is also clear from the ordering parameters discussed above).

4. Summary and conclusions

A survey of the linear microstability properties of the NSTX edge plasma without and with lithium coated PFCs has illuminated several features. First, microtearing appears to be the dominant instability at the pedestal top without lithium. With lithium, this is stabilized by an
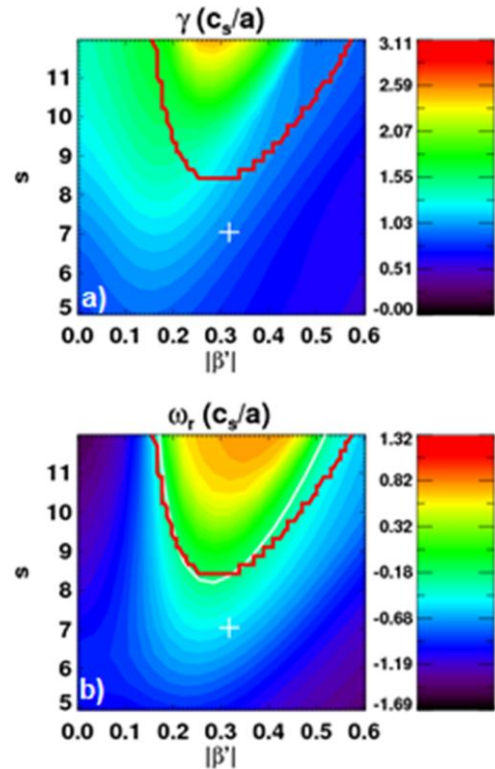
increased density gradient (the decreased collisionality is weakly destabilizing at these parameters). At higher density and pressure gradients, either in the pedestal in the without-lithium case or in the broader region observed to have high gradients with lithium, microtearing and ITG modes are stabilized, and a hybrid TEM/KBM is dominant; this mode is stabilized by pressure gradient at experimental parameters. While the local calculations presented here indicate that KBM onset does not appear to limit the pedestal pressure gradient, future research will employ global gyrokinetic calculations [12] that are necessary to more quantitatively analyze the pedestal region.

While the decrease in transport at the pedestal top and widening of the steep-gradient region observed with lithium appears to be due to the stabilization of microtearing modes by the density gradient as the pedestal grows inwards, it remains unclear how the transport is changed within the pedestal such that ELMs are eliminated and the pedestal is free to grow. ETG modes have been identified as one possible mechanism, since these are calculated to be much more unstable with lithium and hence may provide an additional transport channel that keeps the pressure (and bootstrap current) low near the separatrix. As part of future research, the role of ETG will be explored by performing non-linear simulations in order to quantify how much transport ETG can provide.

References

[1] R. Maingi *et al*, Phys. Rev. Lett. **107** (2011) 145004; R. Maingi *et al*, Nuc. Fusion **52** (2012) 083001.
[2] M.G. Bell *et al*, Plasma Phys. Contr. Fusion **51** (2009) 124054.
[3] D.K. Mansfield *et al*, J. Nucl. Mat. **390-391** (2009) 764.
[4] R. Maingi *et al*, Phys. Rev. Lett. **103** (2009) 075001.
[5] R. Schneider *et al*, Contrib. Plasma Phys. **46** (2006) 3.
[6] J.M. Canik *et al*, J. Nucl. Mat. **415** (2011) S409.
[7] J.M. Canik *et al*, Phys. Plasmas **18** (2011) 056118.
[8] P.B. Snyder *et al*, Phys. Plasmas **9** (2002) 2037.
[9] D.P. Boyle *et al*, Plasma Phys. Contr. Fus. **53** (2011) 10501.
[10] M. Kotschenreuther *et al*, Comput. Phys. Commun. **88** (1995) 128.
[11] P.B. Snyder *et al*, Phys. Plasmas **16** (2009) 056118.
[12] T. Görler *et al*, Phys. Plasmas **18** (2011) 056103.
[13] D. Dickinson *et al*, Phys. Rev. Lett. **108** (2012) 135002.
[14] E.A. Belli and J. Candy, Phys. Plasmas **17** (2010) 112314.
[15] R. Maingi *et al*, Phys. Rev. Lett. **105** (2010) 135004.
[16] W. Guttenfelder, *et al*, Proc. 24th IAEA FEC, San Diego, CA, Oct 8-13 2012, TH/6-1.
[17] C. Bourdelle *et al*, Phys. Plasmas **10** (2003) 2881.
[18] P.B. Snyder *et al*, Nucl. Fusion **51** (2011) 103016.
[19] J.W. Connor, R.J. Hastie, J.B. Taylor, Proc R. Soc. London, Ser. A **365** (1979) 1.
[20] J.M. Greene and M.S. Chance, Nucl. Fusion **31** (1981) 453.
[21] O. Sauter *et al*, Phys. Plasmas **6** (1999) 2834.
[22] S. Koh *et al*, Phys. Plasmas **19** (2012) 07205.
[23] P.B. Snyder and G.W. Hammett, Phys. Plasmas **8** (2001) 744.
[24] P.B. Snyder and H.R. Wilson, Plasma Phys. Control. Fusion **45** (2003) 1671.